Basal Plane Oxygen Exchange of Epitaxial MoS_2 without Edge Oxidation

Signe S. Grønborg[1], Kristbjörg Thorarinsdottir[1], Line Kyhl[1], Jonathan Rodriguez-Fernandez[1], Charlotte E. Sanders[3], Marco Bianchi[2], Philip Hofmann[2], Jill A. Miwa[1,2], Søren Ulstrup[2] and Jeppe V. Lauritsen[1,*]

1. Interdisciplinary Nanoscience Center (iNANO), Aarhus University, Aarhus, Denmark

2. Department of Physics and Astronomy, Aarhus University, Aarhus, Denmark

3. Central Laser Facility, STFC Rutherford Appleton Laboratory, Harwell, United Kingdom

**Corresponding author email: jvang@inano.au.dk*

Abstract

The intentional formation of defects in transition-metal dichalcogenides, such as MoS_2, is an attractive way to modify the electronic and chemical properties of this class of two-dimensional materials. However, the mechanisms and methods available for selective doping or modification of the basal plane must be improved. Here we investigate the process of O defect formation in epitaxial single-layer MoS_2 on Au(111) using scanning tunneling microscopy (STM) and ambient pressure X-ray photoelectron spectroscopy (AP-XPS) during oxidation with O_2 and H_2O gas from low vacuum to the mbar range. Both oxidants result in exchange of S in the upper part of the basal plane with O, in line with air exposure experiments. Temperature-dependent measurements show that this is an activated process with an experimentally estimated reaction barrier of ~0.79 ± 0.20 eV. We surprisingly find that the morphology of the MoS_2 flakes and their edges remain intact in O_2, even for relatively high concentrations of basal plane O exchange, in contrast to the oxidation behavior of exfoliated single-layer MoS_2. From analysis of atom-resolved STM images of the MoS_2 edges, we can attribute this unusual stability to a passivating effect of excess edge sulfur species adsorbed under the sulfiding conditions of the MoS_2 synthesis in H_2S gas. We thus demonstrate that control over pre-sulfidation of the edges, temperature and pressure during oxidation can be used in a fast process to form strongly O doped single-layer MoS_2 with no degradation of the initial shape and edge structure of the epitaxial MoS_2 sheet.

Keywords: *Two-dimensional materials, single-layer MoS_2, O defects, ambient pressure XPS, STM, MoS_2 edges.*

1. Introduction

The introduction of defects in two-dimensional materials is a proven way to engineer new electronic and chemical properties [1, 2]. For example in graphene, functionalization by H or F heteroatoms enables a modification of the electronic and optical properties [3, 4], and novel catalysts were demonstrated based on single metal ions embedded in N-substituted graphene [5]. For single-layer MoS_2, which is interesting due to its direct band gap [6-8], attention to single atom defects as well as extended structural defect has led to interesting discoveries related to electronic structure, charge transport and magnetism (see *e.g.* [9-17]). MoS_2 nanoparticles are also active catalysts for electrochemical hydrogen evolution [18] and Ni and Co promoted MoS_2 has for many years been in service world-wide as the industry-standard catalyst for sulfur removal from crude oil [19, 20]. While it is known that the edges of the single-layer MoS_2 are highly active for catalysis [21, 22], there is now an interest in activation of the basal plane [23, 24]. O incorporation into MoS_2 has been advocated to promote the electrochemical hydrogen evolution reaction (HER) or oxygen reduction reaction (ORR) [25-27]. Motivated by inducing changes in the electronic, physical or catalytic properties of MoS_2, investigations have thus focused on the formation of vacancies, O substitution [28], N or P doping [29, 30], metal heteroatom incorporation [31-33] or functionalization with organic molecules [34]. Direct modification of MoS_2 has mainly been carried out by physical (*e.g.*, sputtering) or chemical modification schemes involving etching in reductive, oxidative or water environments or plasma treatments [35-37]. Etching of MoS_2 in an oxidative environment takes place from the edge sites or at grain boundaries rather than on the pristine basal plane [35, 37-41], and the resulting materials degradation may present a problem for successful basal plane functionalization of devices or nanomaterials consisting of well-defined MoS_2 nanostructures. The free-standing single-layer MoS_2 edges tend to oxidize orders of magnitude faster than the basal plane, and this is in general attributed to the lower coordination and more exposed geometry of the edge Mo atoms compared with the basal plane [42].

In this report we use a combination of ultra-high vacuum (UHV) scanning tunneling microscopy (STM) and ambient-pressure X-ray photoelectron spectroscopy (AP-XPS) to systematically investigate the process for O exchange in epitaxial MoS_2 on Au(111). We find - in contrast to previous observations on free-standing

single-layer MoS_2 - that selective doping of basal plane sulfur sites with oxygen can be obtained at high concentrations without any apparent modification to the edges. From atom-resolved STM images of the post-oxidized structure, we conclude that the low apparent reactivity towards O_2 on the edges is due to a fully sulfur decorated MoS_2 edge configuration formed by *in situ* synthesis in H_2S gas on Au(111) [43, 44], as opposed to MoS_2 sheets obtained from exfoliation. The studies determine a parameter space in temperature and oxygen pressure where one controllably and quickly synthesizes O-functionalized single-layer MoS_2 basal planes on an Au support without affecting the large-scale morphology of single-layer MoS_2 nanostructures. The pristine O-exchanged MoS_2 sheets, thus produced, may open up for new functionalities of MoS_2 and pave the way for further functionalization of the MoS_2 basal plane.

2. Results and Discussion

Structure of pristine epitaxial MoS_2 on Au(111)

The STM image in Figure 1a shows the morphology of the pristine sample used in our experiments consisting of epitaxial single-layer MoS_2 on Au(111) before oxidation. The samples used in our study reflect a partial coverage (~50-70 % of a monolayer (ML)) of MoS_2 synthesized directly in H_2S gas on the gold surface by the cyclic deposition method reported in [43] and [45]. For this coverage, the individual single-layer MoS_2 islands are seen to adopt truncated triangular to almost hexagonal shapes, all oriented with the (0001) surface in parallel with the Au substrate. The size of the individual epitaxial MoS_2 islands on Au(111) can be tuned to larger sizes with single-domain quality by the methods recently reported in [46].

Atom-resolved STM images (Figure 2a) on the top facets reveal a perfect hexagonal atomic lattice, reflecting that the MoS_2 sheet in the as-synthesized state is virtually free of point defects. The bright bumps occasionally seen at random positions on the basal plane (see white arrow in Figure 1a) originate from structures underneath the MoS_2, possibly in the form of trapped Mo. As evident from Figure 1a (and in more detail in Figure 2a), we also observe a large-scale regular hexagonal periodic structure (a moiré) on the basal plane of MoS_2, that arises due to the lattice mismatch and resulting variation in the stacking of the bottom S layers of the MoS_2(0001) lattice against the Au(111) substrate. Direct exposure of the as-synthesized sample

to pure O_2 gas (N5.0 purity) at 10^{-6} mbar at room temperature for 30 min does not affect the pristine appearance of the basal plane sites of the samples as judged from atom-resolved STM. The observation that the basal plane sites are virtually unreactive towards O_2 at room temperature for a short oxygen exposure is consistent with recent studies that showed ultraslow kinetics involved in O substitution on the basal plane after months or even years of air exposure [28]. Likewise, extended annealing at temperatures up to 823 K in the "reducing" environment of ultra-high-vacuum (10^{-10} mbar) did not lead to S desorption and spontaneous formation of defects (vacancies) on the basal plane, confirming the high stability of the MoS_2(0001) basal plane itself. Edge vacancies obtained by exposure to hydrogen gas have been observed previously in STM studies [47-49], but vacancy formation on the basal plane was concluded to be unfavorable in hydrogen here.

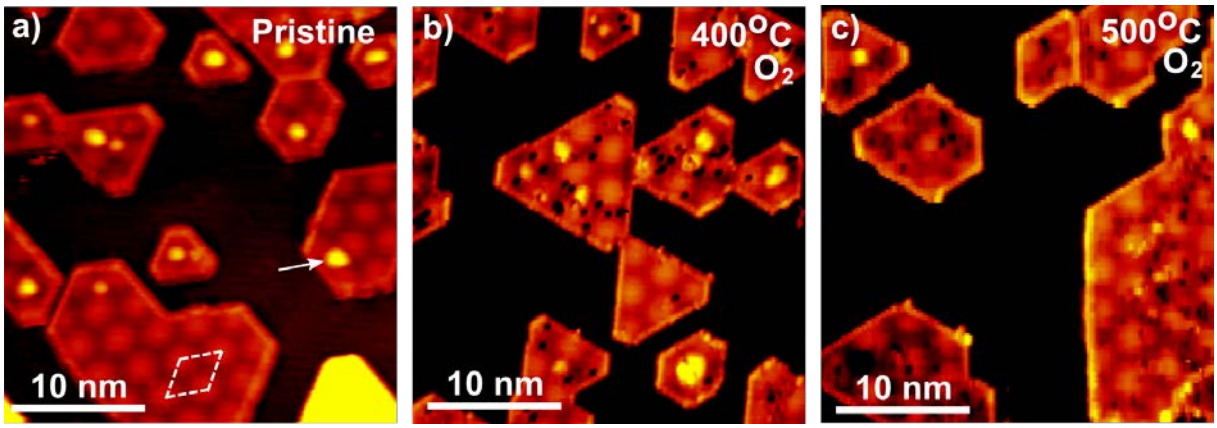

Figure 1: (a) Large-scale STM image of the pristine single-layer MoS_2/Au(111) before O_2 gas exposure. The superimposed rhombic unit cell indicates the periodicity related with the moiré superstructure of the epitaxial MoS2 on Au(111). The white arrow indicates an example of common defect, tentatively associated with Mo underneath the MoS_2 single-layer. STM images of single-layer MoS_2 after exposure to O_2 at P = 1×10^{-6} mbar for 30 min at **(b)** 400ºC and **(c)** 500ºC. All STM images are 30 nm × 30 nm and were recorded at room temperature.

Basal plane oxidation in O_2

While neither oxygen exposure, nor annealing alone leads to the generation of defects in the MoS_2 basal plane, the combination of both does. Figures 1b-c and 2b-d show selected STM images representing the morphology and atomic-scale structure of the MoS_2 islands from a series of oxidation treatments in O_2

(1×10^{-6} mbar for 30 minutes) at increasingly higher temperatures from 200ºC up to 550ºC. It is apparent from the STM image in Figure 2b that a low density of isolated point defects (< 0.5 %) has formed on the basal plane already at 200ºC. The point defects in general appear as dark depressions on the S lattice (Figure 2b). A closer look (Figure 3a and 3b) reveals it as a distortion of the MoS_2 lattice composed of a single central spot on the S lattice, surrounded by a lowering of contrast on the nearby shell of S atoms. This appearance is representative for our low bias, filled state STM images (around V_t = -0.1 V to -0.4 V), but we note that other images recorded at different tunneling parameters revealed the defects without the central spot. We assign these point defects to O atoms substituted into the topmost S lattice positions in the basal plane (denoted as O_S) (Figure 3c). The STM appearance here is only partially matched with recent simulated images of O_S sites in unsupported MoS_2 [28], but the assignment of the defect to O_S here is further supported by our XPS data (see below).

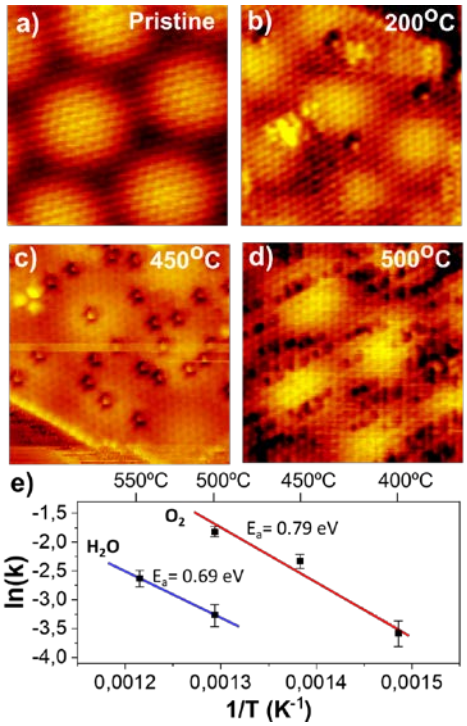

Figure 2: (a) Atom-resolved STM image of the (0001) basal plane of single-layer MoS_2/Au(111) in the pristine state. (**b-d**) STM images of the MoS_2(0001) basal plane recorded after exposure to O_2 at P = 1×10^{-6} mbar for 30 min at (b) 200ºC, (c) 450ºC and (d) 500ºC, respectively. **(e)** Arrhenius plot of the O_S formation rate (**k**) (density/nm^2·s) in O_2 (red curve) and H_2O (blue curve). The error bars reflect the statistical uncertainty in defect counting number (N), estimated by $\sqrt{N}$. STM parameters and image sizes (a): I_t = 1.3

nA, V_t = -0.4 V (6.6 nm x 6.6 nm) , (b): I_t = 1.4 nA, V_t = -0.1 V (7 nm × 7 nm), (c) : I_t = 0.5 nA, V_t =-0.4 V (7 nm × 7 nm), (d): I_t = 0.6 nA, V_t = -0.2 V (7 nm × 7 nm).

The density of O_S during O_2 exposure increases significantly with temperature of the sample as illustrated in Figs. 2c and 2d, reflecting that their formation is an activated process. By variation of the temperature, it is thus possible to control the density of O_S, from less than 0.5% per S basal plane sites to 5.5% for 30 min oxidation at 550 °C. Here it is worth noticing that defects stay separated and that the formed phase thus represents mixed oxy-sulfide $MoS_{2-x}O_x$ with an intact 2D morphology inherited from the epitaxial MoS_2. From the temperature series, we can estimate the activation barrier for the process by plotting the logarithm of the rate of formation (defect density per time unit in $nm^{-2}s^{-1}$) as a function of 1/T in the Arrhenius plot in Fig 2e. Here the slope is a measure of the activation barrier ($-E_a/k_B$), where k_B is Boltzmann's constant. From a fit to the experimental data points, we obtain a value of $E_a = 0.79 \pm 0.20$ eV. This experimental value for the energy barrier is in the lower range compared with theoretical predictions (~1.0 eV [28]), which considered an activated reaction involving a rate-limiting step consisting of SO_2 formation leading to a S vacancy in the topmost S layer of MoS_2. Here, however, we note that certain areas within the moiré superstructure of the epitaxial MoS_2/Au seem to be more susceptible to O_S formations over others (especially for high O_S concentrations, see Figure 2d). Low energy electron diffraction (LEED) studies have shown that the epitaxial single-layer MoS_2 on Au(111) appears on average unstrained in the in-plane direction [50], but a local out-of-plane strain involved in the buckling (and moiré pattern) of the MoS_2 lattice may cause local changes to the reactivity and a lowering of the average barrier. In fact, it has been observed that out-of-plane buckling of MoS_2 can lead to a changed reactivity of the basal plane sites for S vacancy formation [24]. A similar effect caused by the out-of-plane buckling may in our case explain the locally enhanced O_S concentrations in Figure 2d.

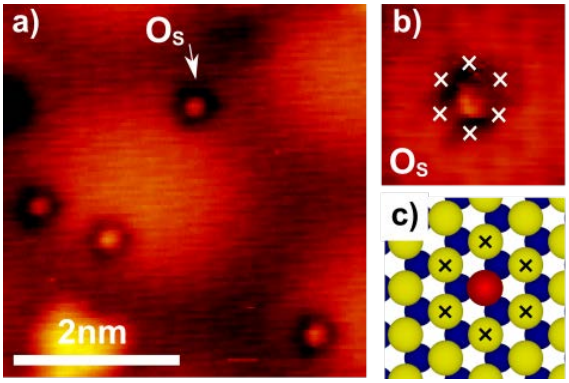

Figure 3: (a) Atom-resolved STM image of O_S sites formed on the (0001) basal plane of MoS_2 by O_2 exposure (V_t = -0.4 V; I_t = 0.5 nA) **(b)**. Zoom-in on a single O_S site observed in STM. The O_S site is resolved in STM as a perturbation of the lattice at the defect site and the surrounding shell of S atoms. A central spot is visible here, but we note that this appearance was observed to be highly dependent on tip state and tunneling conditions. The superimposed crosses indicate neighboring S lattice sites. **(c)** Ball model representation of the O_S site and surrounding six S sites, again indicated by the crosses. (S= Yellow, O = Red, Mo = Blue).

AP-XPS Studies of O Exchange in MoS_2/Au at 0.1 mbar O_2 pressure

Using AP-XPS we can spectroscopically follow the O_S formation of the epitaxial MoS_2/Au while annealing at a higher oxidation pressure (mbar range), relevant to ambient pressure 2D material processing conditions. Figure 4 displays the Mo3d and S2p doublet spectra of the Au(111)-supported SL MoS_2 together with the O1s peak recorded *in situ* as we gradually heat the sample from room temperature (25ºC) to 350ºC in a O_2 partial pressure of 0.1 mbar. No other elements (apart from Au) were present in the XPS spectra. Initially at room temperature in O_2, the sample spectra show the XPS signature of pristine epitaxial MoS_2/Au with a binding energy of the $Mo3d_{5/2}$ peak of 229.3 eV reflecting Mo in the +4 state (blue), and a broadened S2p doublet (yellow) with the $S2p_{3/2}$ component located at 162.2 eV (see table S1) [44, 46]. Furthermore, a low intensity S2p component (red, labelled high BE) could be seen with the $S2p_{3/2}$ component at a significantly higher binding energy of 164.3 eV. For the O1s spectrum recorded in 0.1 mbar O_2 at room temperature in Figure 4, we observe an O_2(g) peak due to the O_2 gas in the volume under the analyzer located at high binding energies (> 536 eV) [51] together with a low intensity peak at lower binding energy reflecting a surface O species. The initial surface O peak (red) can be fitted by a single O1s binding energy component at

529.7 eV. We associate this peak to a low initial concentration of substituted O_S species originating from transfer in air from the vacuum suitcase to the beamline or induced by the first transient period in oxygen gas in the AP-XPS chamber, in line with the findings for O exchange at room temperature [28].

When the temperature of the sample, kept in 0.1 mbar O_2, increases to 100ºC and then to 200ºC in Figure 4, we observe growth of the surface O1s peak (see XPS quantification in Figure S1), indicating that O_S sites are now being formed in agreement with the STM experiments (Figure 2). On the other hand, the Mo3d spectra in Figure 4 are, not strongly affected at these temperatures. The unshifted Mo3d peak is, however, consistent with O substitution on the S lattice, since the gradual replacement of S with O in the $MoS_{2-x}O_x$ phase does not change the +4 oxidation state of Mo, and one can therefore expect that the chemical shift is similar. For the S2p doublet peak we see small changes reflected by the emergence of a lower binding energy peak structure (green) with the $S2p_{3/2}$ located 1.2 eV lower than the main peak at E_b = 161.0 eV at 200ºC and an intensity change of the high binding energy structure 164.3 eV (see also Figure S1). We tentatively assign these changes in the S2p peak to modified S atom species arising due to the oxidation of the basal plane of MoS_2. The atom-resolved STM image in Fig 3b of the O_S site indeed shows that not only the central O site is affected by the substitution of O, but also the six surrounding nearest neighbor S atoms are modified electronically (the dark halo around the O_S site in Figure 3b).

From 200ºC we can also observe the growth of another O peak located at 528.4 eV (blue) in the O1s spectrum in Figure 4. This indicates the onset of oxidation of the MoS_2 phase into a Mo oxide in the O_2 gas. When the sample temperature is further raised to 300ºC in 0.1 mbar O_2 the oxidation becomes more apparent, indicated by the emergence of a new Mo3d doublet peak structure shifted 2.8 eV from the former Mo3d peak positions. This shift is a change in the oxidation state of Mo from Mo^{4+} to Mo^{6+} [52]. For the O1s spectra at 300ºC and above, the peak assigned to O_S is now gone and instead we only see a single peak (blue) at the lower binding energy of 528.4 eV. In the corresponding S2p spectra, a complete loss of sulfur signal is observed. Overall, the XPS data therefore reflects that full degradation of the single-layer MoS_2 structure into MoO_3 has taken place at 300ºC. To get a more precise estimate for the onset temperature for MoO_3 formation, we performed a temperature programmed AP-XPS measurement in 0.1 mbar O_2 focused on the

$Mo3d_{5/2}$ signal intensity (Supplementary Figure S3). Here we see a stable Mo^{4+} component as a function of temperature, consistent with the gradual O_S formation, until MoO_3 formation finally initiates at an onset temperature of ~280ºC.

The formation of Mo oxide can also be detected in the oxidation experiments at lower pressure with STM, although its formation is shifted to higher temperatures. Above 500ºC, we see a mixed surface morphology consisting of either well-defined $MoS_{2-x}O_x$ islands or particles that have completely converted into a structure that bears strong resemblance to a mixture of MoO_3/MoO_2 on Au(111) (Figure S3) [53]. The difference in the temperature onset for MoO_3 formation between STM and AP-XPS experiments is explained by the difference in chemical potential of O_2 for the pressures used in the two separate experiments. Between the highest two temperatures, 300ºC and 350ºC in the 0.1 mbar O_2 atmosphere, the AP-XPS data for Mo3d (Figure 4) shows a significant loss of Mo on the surface. A similar loss of material is detected in the low-pressure STM oxidation experiment, but only for temperature above 550ºC. In both cases, we ascribe this to evaporation of Mo due to the high volatility of the Mo trioxide phase [54].

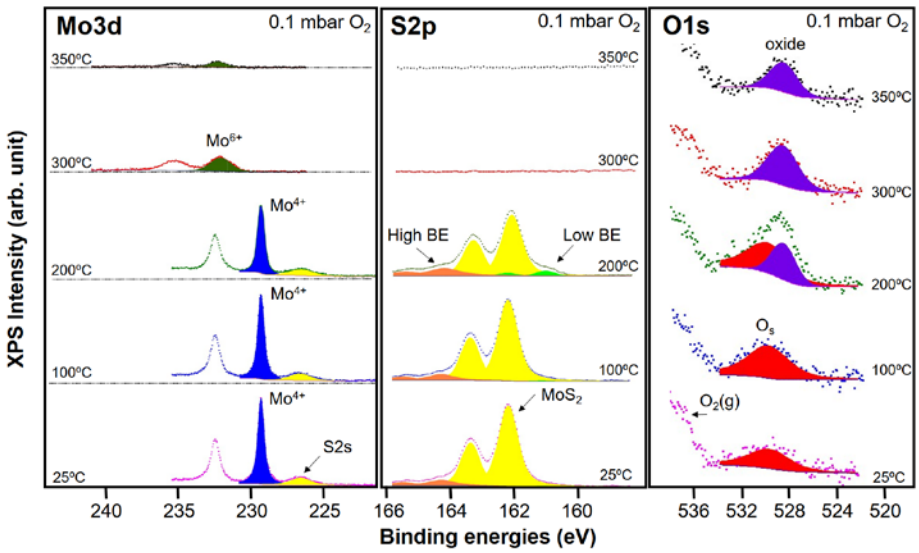

Figure 4: AP-XPS data of MoS_2/Au(111) recorded while increasing the temperature from room temperature to 350ºC in 0.1mbar O_2. The XPS data shows the regions containing the Mo3d, S2p and O1s peaks, respectively and the temperature is indicated for each spectrum. The intensity scale is relative to the first spectrum for each segment. In the O1s segment, the gas phase peak (O_2(g)) was located just outside the O1s region at higher energies. Peak energies are obtained from peak fitting and the peak positions are listed in

Table S1. The quantification of the peak areas of all peak components in Mo3d, S2p and O1s can be found in Figure S1. Photon energies were 335 eV (S2p), 420 eV (Mo3d) and 820 eV (O1s), respectively.

Basal plane Oxidation in Water Vapor

We have then investigated the oxidation of the MoS_2 flakes with H_2O vapor as the oxidizing gas. Figure 5a-d shows a series of STM images of the MoS_2/Au(111) sample after exposure to H_2O at 1×10^{-6} mbar for 30 min at the indicated temperature. The STM images at 500ºC again reveal the formation of a low concentration of point-like defects on the MoS_2 basal plane. Figure 5d shows an atom-resolved STM image of a MoS_2 layer with a number of the dark point defects that match the assignment of the O_S from Figure 3. We therefore conclude that it is also possible to induce the thermal formation of O_S sites using H_2O as the oxidizing gas. However, the temperature at which we begin to detect a significant number of defects seems to be shifted considerably higher to 500ºC, compared with O_2. This overall indicates that the MoS_2/Au is less prone to O exchange in H_2O gas than in O_2.

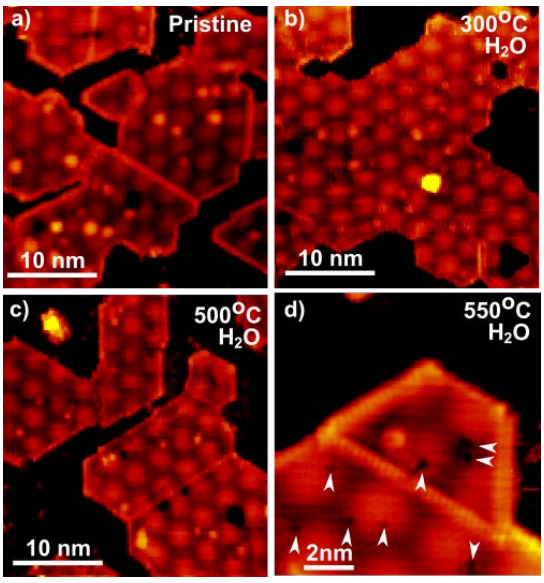

Figure 5: (a) Large-scale STM image of the single-layer MoS_2/Au(111) before H_2O exposure. STM images of single-layer MoS_2 after exposure to H_2O at P = 1×10^{-6} mbar for 30 min at **(b)** 300ºC and **(c)** 500ºC. Images a-c are 30 nm × 30 nm **(d)** Atom-resolved 10 nm × 10 nm STM image of single-layer MoS_2 after H_2O exposure at 550ºC. The superimposed arrowheads indicate the position of dark depressions on the S lattice positions associated with O_S formation. I_t = 0.4 nA, V_t = -1.1 V. All STM images were recorded at room temperature.

The corresponding AP-XPS experiment confirms that H_2O is a milder oxidant than O_2. Figure 6 illustrates the Mo3d, S2p and O1s photoemission spectra recorded *in situ* in 0.1 mbar H_2O vapor in the temperature range from room temperature to 425 ºC. The initial Mo3d peak and S2p peaks at room are again in line with pristine MoS_2/Au temperature (see binding energies in Table S1). Both their position and peak structure remain stable up to a temperature of 350ºC, reflecting that MoS_2 is stable in H_2O up to this temperature. The O1s spectrum recorded in 0.1mbar H_2O is more complicated than in O_2 as it can be fitted with three peaks in the temperature interval up to 350 ºC. The sharp peak at 535.6 eV is the gas phase H_2O(g) peak, whereas the peak at 532.8 eV is consistent with adsorbed water on the surface [55]. As we heat the sample, we see a decrease of the adsorbed water peak (see also Figure S4), as expected, and a corresponding growth of a lower binding energy peak at 531.2 eV. There is no indication for a peak at the O_S peak position (529.7 eV) detected with XPS in the case of O_2 (Figure 4). However, considering that the O exchange takes place in H_2O and that this peak grows with temperature, we can still assign the 531.2 eV peak to formation of O_S sites if we assume that a hydroxyl group consisting of a substituted O and an adsorbed H is formed instead, *i.e.* a O_S-H group. In fact, the position of O1s peak corresponding to the O_S-H is shifted by ~1.5 eV to higher binding compared with O_S. This shift has a magnitude typical for the chemical shift observed in O1s XPS spectra for hydroxyl groups on many oxides surfaces [55]. Returning to our atom-resolved STM images for O defect sites formed in O_2 (Figure 3a) and H_2O (Figure 5d), the STM images do not allow us to conclude about a specific STM signature associated with either O_S or O_S-H sites, respectively, as we in general see a variety of dark site contrasts in both cases. Future low temperature STM and non-contact AFM imaging experiments can possibly reveal quantitative contrast differences between a clean O_S and a hydroxylated site.

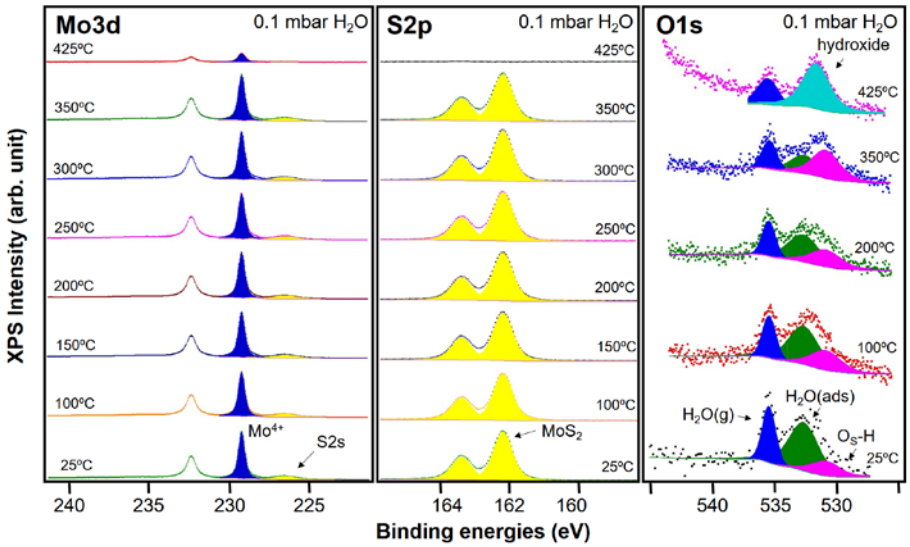

Figure 6: AP-XPS data of MoS_2/Au(111) recorded while increasing the temperature from room temperature to 425ºC in 0.1mbar H_2O. The data shows the regions containing the Mo3d, S2p and O1s peaks, respectively and the temperature is indicated for each spectrum. The intensity scale is relative to the first spectrum for each segment. In the O1s segment, the gas phase peak (O_2(g)) was located just outside the O1s region at higher energies. Peak energies are obtained from peak fitting and the peak positions are listed in Table S1. The quantification of the peak areas of all peak components in Mo3d, S2p and O1s can be found in Figure S4. Photon energies were 335 eV (S2p), 420 eV (Mo3d) and 650 eV (O1s), respectively.

At subsequently higher temperatures up to 425ºC in Figure 6 we see a significant loss of Mo and total elimination of S from the surface, which we assign to degradation of the 2D MoS_2 and subsequent evaporation of oxide from the surface. In comparison, the degradation temperature was 280ºC in 0.1 mbar O_2. Unlike heating in O_2, we see that remnant Mo at high temperature stays in the Mo^{4+} state in H_2O with a $Mo3d_{5/2}$ peak at 229.3 eV. In the corresponding O1s spectra in H_2O at 425 ºC, the position of a new peak at 531.8 eV is consistent with formation of a oxy-hydroxide formed by the water exposure, such as $MoO(OH)_2$, where Mo is in the 4+ oxidation state [52].

From the STM data, we have again counted the number for defects formed as a function of temperature to obtain a rate of formation and added these to the Arrhenius plot in Figure 2e (H_2O data shown in blue). The data points were reduced to two in the case of H_2O due to the smaller temperature window in which the O_S sites are formed in substantial numbers. In the Arrhenius plot in Figure 2e the shift in the position of the blue line (H_2O) on the vertical (log) axis compared with the red line (O_2) is due to the lower rate of formation in

H_2O vapor than in O_2. The slope of the blue line in H_2O, on the other hand, is still a measure of the activation barrier, and the near parallel orientation of the blue line (slope corresponding to 0.69 ± 0.20 eV) compared with the red line (0.79 eV) suggest that the activation barriers are not very different within the error bar for each oxidant.

MoS_2 edge stability in O_2 and H_2O

The series of STM images in Figure 1 and Figure 5 reveal that the sharply defined morphology of the individual MoS_2 islands remains surprisingly unaffected by heating in H_2O and O_2, even for high concentrations of O_S defects (for example Figure 1c at 500ºC). An atom-resolved STM image of the edges termination of an oxidized MoS_2 island is shown in Figure 7a. Interestingly, this contrasts the rugged morphology often seen in microscopy images for exfoliated or chemical vapor deposition (CVD) grown MoS_2 flakes after exposure to oxidative conditions in ambient O_2 or H_2O [37, 56, 57]. Our STM observations thus show that the MoS_2 islands on Au(111) are significantly less susceptible to oxidation at the edges than on the basal plane under the conditions used here. Modelling work using DFT has shown that the exposed edges should be highly reactive towards detrimental oxidation using molecular O_2 due to a combination of favorable kinetics and a thermodynamic driving force for MoO_3 formation at edge sites [42]. These studies, however, assumed an edge termination in a lower sulfided state with a 50% S coverage, which in general may be more reactive than the fully sulfided MoS_2 edges present in our case [58, 59]. To see this, we refer to previous STM experiments that have determined that the hexagonal MoS_2 sheets in Figure 1a are terminated exclusively by two types of edges, the low-index $(\bar{1}010)$ S-edge and $(10\bar{1}0)$ Mo-edge (zig-zag) edge types, illustrated in the ball model in Figure 7b [21, 47]. However, the resulting edges of the hexagonal MoS_2 islands in Figure 1a are not bulk-terminated versions of the MoS_2 edges obtained from a simple truncation of a MoS_2 sheet since additional S will adsorb during the *in situ* synthesis in H_2S on the under-coordinated edge sites of the "naked" Mo edge (Figure 7b). Thus, in the fully sulfided state, the MoS_2 edge types in the hexagon expose a fully sulfided Mo edge with S_2 dimers terminating the Mo-edge (100%), as shown in Figure 7c [21, 60, 61] and a corresponding 100% S coverage on the S edge, respectively [62]. This assignment was previously done by a detailed comparison of the STM contrast with simulations of the local-

density of states from DFT modelling of all type of edges. In comparison, the atom-resolved STM image in Figure 7a of the edges of a hexagonal MoS_2 island imaged after O_2 exposure show no signs of a different edge structure. Specifically, for the Mo edge in Figure 7a, the edge protrusions are imaged *out-of registry* with the basal plane S lattice (white markers), as for the fully sulfided Mo edge, and a bright brim originating from an electronic edge state [63] is clearly seen in the second row behind the Mo edge. We note that the theoretical STM simulations in that study showed that the STM image contrast on the Mo edge is dominated by electronic effects, so that the interstitial region between S_2 dimers is imaged bright, and hence out of registry (compare figure 7a and ball model in figure 7b). Furthermore, a characteristic double period along the row of Mo edge protrusions originating from pairing of S_2 dimer pairs [21] is also detected. This Mo edge after O_2 exposure is thus imaged qualitatively and quantitatively identical with unexposed fully sulfided 100% S Mo edge in the pristine MoS_2. For the S edge after O_2 exposure imaged in Figure 7a, the edge protrusions are *in registry* (grey markers) and a brim is seen in the row behind the edge. These are again unchanged signatures that reflect a fully sulfided 100% S edge (Figure 7c). We can therefore conclude that the full S coverage is kept on the edges even when a substantial amount of O_S sites are formed.

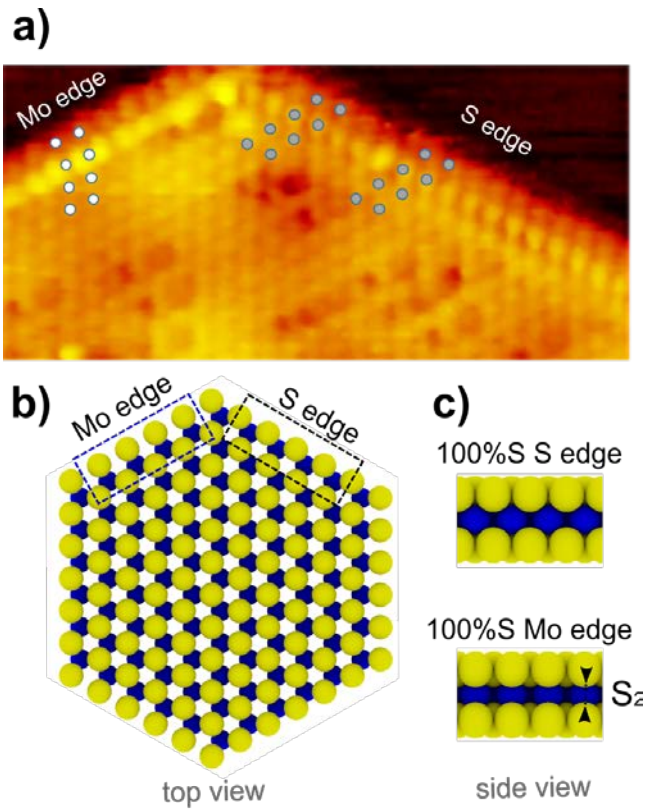

Figure 7: a) Atom-resolved STM image (7 nm × 3.5 nm) of an MoS_2 island with O_S defects on the basal plane formed at 500ºC in O_2 illustrating a 120º corner of a hexagonal island with the two types of edges (S and Mo edge) exposed, respectively. Imaging parameters: I_t = 0.6 nA, V_t =-0.2 V. The superimposed markers illustrate the *out-of-registry* position of edge protrusions on the Mo edge (white markers) and *in-registry* position on the S edge (grey markers) with respect to the basal plane sulfur lattice positions, respectively **b)** Ball model of a hypothetical single-layer MoS_2 hexagonal island terminated by the two low-index Mo edges and S edges, respectively. The edges expose the actual sulfur coverages and exact edge sections shown in side view are marked with a dashed rectangle. **c**) Side view ball models show the structure of fully sulfided (100% S covered) S edges and S_2 dimer (100%S) terminated Mo edge reflected in the experimental image, as determined in previous STM studies [21, 61, 63, 64]. We note that the out-of-registry position in the STM image on the Mo edge is an electronic effect where the region in between S_2 dimers is imaged bright.

The slow evolution of the O1s peak in the AP-XPS data, furthermore suggests that edge oxidation is not predominant in the 0.1 mbar atmospheres of O_2 and H_2O, respectively, until fast degradation of the 2D sheet into MoO_3 sets in at the highest temperature (Figs. 4 and 6). We therefore attribute the apparent inactivity of the MoS_2 edges to the fully sulfur saturated state of the edges (Figure 6c), obtained when they are synthesized in excess H_2S gas. On the Mo edge, this particular stability may be linked with the formation of particularly stable S_2 dimer species (disulfide) terminating the edges (see Figure 7c) [59, 65]. As a contributing factor, we note that recent theoretical modelling has shown that the Au support slightly stabilizes the extra sulfur atom in the S_2 dimer on the Mo edge compared to unsupported MoS_2. [66] The effect is thus demonstrated here for Au supported MoS_2, and it should be verified for single-layer MoS_2 supported on other substrates such as SiO_2 or graphene. Future work, using *e.g.* DFT modelling, might be also used to shed light on whether edge oxidation is inhibited for the 100% S-saturated MoS_2 edges based on thermodynamics related with removal of the edge S, or whether kinetics due to lack of sites for O_2 adsorption on the fully sulfided edge structures is the origin of the stability of the MoS_2/Au system towards oxidative attack on the MoS_2 edges. Such insight may help provide viable ways of functionalizing the basal plane of MoS_2 in oxidative environments.

3. Conclusions

We have investigated selective O exchange on the basal plane sites of Au(111) supported epitaxial MoS_2 single-layers resulting from O_2 and H_2O exposure at elevated temperature. Using a combination of STM and ambient pressure XPS performed at varying temperature and pressure, we find that O exchange is an activated process with an energy barrier of ~0.8 eV, and that this value is similar within the uncertainty of the experiment for the process taking place in O_2 gas or H_2O gas. Atom-resolved STM images reveal O as single defects located on isolated positions on the upper S lattice of MoS_2, in accordance with recent literature [28]. Unlike other reports on the air stability of single-layer MoS_2, we find that the edges are protected from oxidative attack, even for high O exchange levels on the basal plane. We link this passivation of the edges to the fully sulfided edges that are formed during *in situ* synthesis in H_2S. Only at relatively strong oxidation potentials, such as heating to 280ºC in 0.1 mbar O_2, do we see degradation of the MoS_2 and the gradual formation of oxide phases. Future studies could be aimed at clarifying the effect of ambient air consisting of both O_2 and H_2O, e.g. to link these studies to ambient air exposure studies. In our case, we propose that pre-saturation with sulfur combined with accurate control over temperature and O_2 pressure is a viable method to obtain selective O functionalization of the basal plane of MoS_2. The method may be used to generate O-modified MoS_2 in a fast and controllable way, but the changed chemistry of the O sites in MoS_2 could also provide interesting possibilities for catalysis and open for further pathways leading to additional functionalization of the basal plane sites with molecules or other heteroatoms.

4. Methods

MoS_2/Au synthesis: Single-layer MoS_2 was grown on a Au(111) sample using procedures reported elsewhere [43, 45]. In short, Mo is evaporated onto a clean Au(111) in a H_2S atmosphere (~5×10^{-6} mbar) followed by annealing at 570ºC in the same H_2S atmosphere. The single-layer MoS_2 sample coverages used here were approximately 50-70% of a monolayer. Scanning tunneling microscopy was performed with an Aarhus STM operated at room temperature using etched W tips. *Oxidation (low pressure):* After the synthesis and initial characterization, the samples were heated in a pressure of 1×10^{-6} mbar of O_2 or H_2O gas, respectively for 30 minutes. The data was collected in the temperature range from 200-550ºC in an accumulative manner. On the temperature ramp down the sample remained in the gaseous environment, which was pumped out once the sample reached 173ºC. The sample was then flash-annealed in ultra-high vacuum at ~200ºC and imaged at room temperature. To obtain the rate of formation, the accumulated number of O_S sites per area was counted from atom resolved STM images after each heating stage. Gases were supplied to the vacuum through leak valves from a lecture bottle with a nominal purity better than 99.8% for H_2S (N2.8) and 99.9999% for O_2 (N5.0)

X-ray photoelectron spectroscopy: The AP-XPS measurements were carried out at beamline 9.3.2 at the Advanced Light Source in Berkeley, USA. The spectra were obtained using a photon energy of 335 eV (S2p), 420 eV (Mo3d), 820 eV (O1s, O_2 series) and 650 eV (O1s, H_2O series), respectively. The pressure during AP-XPS was 0.1 mbar for both O_2 and H_2O. For the AP-XPS data the single-layer MoS_2/Au(111) samples were grown in a dedicated growth chamber and stored in a vacuum suitcase under static vacuum for transportation. The sample was exposed to ambient conditions shortly during sample mounting and extraction, which may explain the initial oxygen content of the sample as measured in the O1s signal. The sample was flash-annealed to ~200ºC under ultra-high vacuum at the beamline prior to the AP-XPS measurements. The XPS spectra were fitted with a Shirley background and a Gaussian/Lorentzian convolution peak shape. The only exception was the O1s spectrum of the O_2 series, which was fitted to a linear background to better account for the gas peak situated at the high binding energy cut-off. Peak

positions are listed in Table S1. Peak positions for Mo3d and S2p were directly calibrated to the Fermi level, whereas the O1s in the H_2O series were calibrated to the Au4f peak.

Acknowledgements: We gratefully acknowledge grants from the VILLUM foundation, the Center for Dirac Materials (VCDM, Grant No. 11744), the VILLUM Young Investigator program (Grant No. 15375) and VILLUM project (Grant No. 13264, JVL). We also acknowledge Innovation Fund Denmark (CAT-C project). We acknowledge beamtime received at beamline 9.3.2 of the Advanced Light Source (ALS), Berkeley, which is a DOE Office of Science User Facility under contract no. DE-AC02-05CH11231. We thank Ethan Crumlin at the ALS for advice and help with AP-XPS experiments. J.M acknowledges the Aarhus University Research Foundation, and the Danish Council for Independent Research, Natural Sciences under the Sapere Aude program (Grants No. DFF-6108- 00409).

Description of Supporting Information: Table containing XPS Binding Energies; Quantitative analysis of XPS data for O_2 and H_2O experiments, XPS spectra and Temperature Programmed XPS study of MoS_2 conversion into oxide in O_2; STM images of Mo oxide phases formed by decomposition of MoS_2 in O_2.

References

[1] Banhart F, Kotakoski J and Krasheninnikov A V 2011 *ACS Nano* **5** 26-41
[2] Lin Z, Carvalho B R, Kahn E, Lv R, Rao R, Terrones H, Pimenta M A and Terrones M 2016 *2D Materials* **3** 022002
[3] Balog R, Jorgensen B, Nilsson L, Andersen M, Rienks E, Bianchi M, Fanetti M, Lægsgaard E, Baraldi A, Lizzit S, Sljivancanin Z, Besenbacher F, Hammer B, Pedersen T G, Hofmann P and Hornekaer L 2010 *Nat. Mater* **9** 315-9
[4] Walter A L, Sahin H, Jeon K-J, Bostwick A, Horzum S, Koch R, Speck F, Ostler M, Nagel P, Merz M, Schupler S, Moreschini L, Chang Y J, Seyller T, Peeters F M, Horn K and Rotenberg E 2014 *ACS Nano* **8** 7801-8
[5] Deng D, Chen X, Yu L, Wu X, Liu Q, Liu Y, Yang H, Tian H, Hu Y, Du P, Si R, Wang J, Cui X, Li H, Xiao J, Xu T, Deng J, Yang F, Duchesne P N, Zhang P, Zhou J, Sun L, Li J, Pan X and Bao X 2015 *Science Advances* **1**
[6] Splendiani A, Sun L, Zhang Y B, Li T S, Kim J, Chim C Y, Galli G and Wang F 2010 *Nano Lett.* **10** 1271-5
[7] Mak K F, Lee C, Hone J, Shan J and Heinz T F 2010 *Phys. Rev. Lett.* **105** 4
[8] Chhowalla M, Shin H S, Eda G, Li L J, Loh K P and Zhang H 2013 *Nat. Chem.* **5** 263-75
[9] Chen Y, Huang S, Ji X, Adepalli K, Yin K, Ling X, Wang X, Xue J, Dresselhaus M, Kong J and Yildiz B 2018 *ACS Nano* **12** 2569-79
[10] Hong J, Hu Z, Probert M, Li K, Lv D, Yang X, Gu L, Mao N, Feng Q, Xie L, Zhang J, Wu D, Zhang Z, Jin C, Ji W, Zhang X, Yuan J and Zhang Z 2015 *Nat. Commun.* **6** 6293
[11] Zhang Z, Zou X, Crespi V H and Yakobson B I 2013 *ACS Nano* **7** 10475-81

[12] Yu Z, Pan Y, Shen Y, Wang Z, Ong Z-Y, Xu T, Xin R, Pan L, Wang B, Sun L, Wang J, Zhang G, Zhang Y W, Shi Y and Wang X 2014 *Nat. Commun.* **5** 5290
[13] Mann J, Ma Q, Odenthal P M, Isarraraz M, Le D, Preciado E, Barroso D, Yamaguchi K, von Son Palacio G, Nguyen A, Tran T, Wurch M, Nguyen A, Klee V, Bobek S, Sun D, Heinz T F, Rahman T S, Kawakami R and Bartels L 2013 *Adv. Mat.* **26** 1399-404
[14] Song S H, Joo M-K, Neumann M, Kim H and Lee Y H 2017 *Nat. Commun.* **8** 2121
[15] Noh J-Y, Kim H and Kim Y-S 2014 *Phys. Rev. B* **89** 205417
[16] Hu Z, Wu Z, Han C, He J, Ni Z and Chen W 2018 *Chem. Soc. Rev.* **47** 3100-28
[17] Zhang J, Soon J M, Loh K P, Yin J H, Ding J, Sullivian M B and Wu P 2007 *Nano Lett.* **7** 2370-6
[18] Laursen A B, Kegnæs S, Dahl S and Chorkendorff I 2012 *Energy & Environmental Science* **5** 5577-91
[19] Hansen L P, Ramasse Q M, Kisielowski C, Brorson M, Johnson E, Topsøe H and Helveg S 2011 *Angew. Chem. Int. Ed.* **50** 10153-6
[20] Lauritsen J V, Kibsgaard J, Olesen G H, Moses P G, Hinnemann B, Helveg S, Nørskov J K, Clausen B S, Topsøe H, Lægsgaard E and Besenbacher F 2007 *J. Catal* **249** 220-33
[21] Lauritsen J V, Kibsgaard J, Helveg S, Topsøe H, Clausen B S and Besenbacher F 2007 *Nat. Nanotechnol.* **2** 53-8
[22] Kibsgaard J, Chen Z B, Reinecke B N and Jaramillo T F 2012 *Nat. Mater* **11** 963-9
[23] Li G, Zhang D, Qiao Q, Yu Y, Peterson D, Zafar A, Kumar R, Curtarolo S, Hunte F, Shannon S, Zhu Y, Yang W and Cao L 2016 *J. Am. Chem. Soc.* **138** 16632-8
[24] Li H, Tsai C, Koh A L, Cai L L, Contryman A W, Fragapane A H, Zhao J H, Han H S, Manoharan H C, Abild-Pedersen F, Norskov J K and Zheng X L 2016 *Nat. Mater* **15** 1
[25] Xie J, Zhang J, Li S, Grote F, Zhang X, Zhang H, Wang R, Lei Y, Pan B and Xie Y 2013 *J. Am. Chem. Soc.* **135** 17881-8
[26] Zhou J, Fang G, Pan A and Liang S 2016 *ACS Applied Materials & Interfaces* **8** 33681-9
[27] Huang H, Feng X, Du C, Wu S and Song W 2015 *Journal of Materials Chemistry A* **3** 16050-6
[28] Pető J, Ollár T, Vancsó P, Popov Z I, Magda G Z, Dobrik G, Hwang C, Sorokin P B and Tapasztó L 2018 *Nat. Chem.* **10** 1246–51
[29] Azcatl A, Qin X, Prakash A, Zhang C, Cheng L, Wang Q, Lu N, Kim M J, Kim J, Cho K, Addou R, Hinkle C L, Appenzeller J and Wallace R M 2016 *Nano Lett.* **16** 5437-43
[30] Nipane A, Karmakar D, Kaushik N, Karande S and Lodha S 2016 *ACS Nano* **10** 2128-37
[31] Hakala M, Kronberg R and Laasonen K 2017 *Sci Rep* **7** 15243
[32] Liu G, Robertson A W, Li M M-J, Kuo W C H, Darby M T, Muhieddine M H, Lin Y-C, Suenaga K, Stamatakis M, Warner J H and Tsang S C E 2017 *Nat. Chem.* **9** 810
[33] Zhang H, Yu L, Chen T, Zhou W and Lou X W 2018 *Advanced Functional Materials* **0** 1807086
[34] Ding Q, Czech K J, Zhao Y, Zhai J, Hamers R J, Wright J C and Jin S 2017 *ACS Applied Materials & Interfaces* **9** 12734-42
[35] Wang Z, Li Q, Xu H, Dahl-Petersen C, Yang Q, Cheng D, Cao D, Besenbacher F, Lauritsen J V, Helveg S and Dong M 2018 *Nano Energy* **49** 634-43
[36] Ye G, Gong Y, Lin J, Li B, He Y, Pantelides S T, Zhou W, Vajtai R and Ajayan P M 2016 *Nano Lett.* **16** 1097-103
[37] Walter T N, Kwok F, Simchi H, Aldosari H M and Mohney S E 2017 *Journal of Vacuum Science & Technology B* **35** 021203
[38] Roberto C L, Rafik A, Santosh K C, Ji-Young N, Christopher M S, Diego B, Chenxi Z, Julia W P H, Robert M W and Kyeongjae C 2017 *2D Materials* **4** 025050
[39] Spychalski W L, Pisarek M and Szoszkiewicz R 2017 *The Journal of Physical Chemistry C* **121** 26027-33
[40] Gao J, Li B, Tan J, Chow P, Lu T-M and Koratkar N 2016 *ACS Nano* **10** 2628-35
[41] Taeg Yeoung K, Areum J, Wontaek K, Jinhwan L, Youngchan K, Jung Eun L, Gyeong Hee R, Kwanghee P, Dogyeong K, Zonghoon L, Min Hyung L, Changgu L and Sunmin R 2017 *2D Materials* **4** 014003
[42] Martincová J, Otyepka M and Lazar P 2017 *Chemistry – A European Journal* **23** 13233-9

[43] Sørensen S G, Füchtbauer H G, Tuxen A K, Walton A S and Lauritsen J V 2014 *ACS Nano* **8** 6788-96
[44] Bruix A, Füchtbauer H G, Tuxen A K, Walton A S, Andersen M, Porsgaard S, Besenbacher F, Hammer B and Lauritsen J V 2015 *ACS Nano* **9** 9322-30
[45] Grønborg S S, Ulstrup S, Bianchi M, Dendzik M, Sanders C E, Lauritsen J V, Hofmann P and Miwa J A 2015 *Langmuir* **31** 9700-6
[46] Bana H, Travaglia E, Bignardi L, Lacovig P, Sanders C E, Dendzik M, Michiardi M, Bianchi M, Lizzit D, Presel F, Angelis D D, Apostol N, Das P K, Fujii J, Vobornik I, Larciprete R, Baraldi A, Hofmann P and Lizzit S 2018 *2D Materials* **5** 035012
[47] Helveg S, Lauritsen J V, Lægsgaard E, Stensgaard I, Nørskov J K, Clausen B S, Topsøe H and Besenbacher F 2000 *Phys. Rev. Lett.* **84** 951-4
[48] Tuxen A, Kibsgaard J, Gøbel H, Lægsgaard E, Topsøe H, Lauritsen J V and Besenbacher F 2010 *ACS Nano* **4** 4677-82
[49] Grønborg S S, Salazar N, Bruix A, Rodríguez-Fernández J, Thomsen S D, Hammer B and Lauritsen J V 2018 *Nat. Commun.* **9** 2211
[50] Grønborg S S, Ulstrup S, Bianchi M, Dendzik M, Sanders C E, Lauritsen J V, Hofmann P and Miwa J A 2015 *Langmuir* **31** 9700-6
[51] Yamamoto S, Bluhm H, Andersson K, Ketteler G, Ogasawara H, Salmeron M and Nilsson A 2008 *Journal of Physics-Condensed Matter* **20** 184025
[52] Brox B and Olefjord I 1988 *Surface and Interface Analysis* **13** 3-6
[53] Salazar N, Beinik I and Lauritsen J V 2017 *Phys. Chem. Chem. Phys* **19** 14020-9
[54] Gulbransen E A, Andrew K F and Brassart F A 1963 *Journal of the Electrochemical Society* **110** 242-3
[55] Bluhm H 2010 *J. Electr. Spectr. Rel. Phenom.* **177** 71-84
[56] Zhang X, Jia F, Yang B and Song S 2017 *The Journal of Physical Chemistry C* **121** 9938-43
[57] Budania P, Baine P, Montgomery J, McGeough C, Cafolla T, Modreanu M, McNeill D, Mitchell N, Hughes G and Hurley P 2017 *MRS Communications* **7** 813-8
[58] Tsai C, Abild-Pedersen F and Nørskov J K 2014 *Nano Lett.* **14** 1381-7
[59] Raybaud P, Hafner J, Kresse G, Kasztelan S and Toulhoat H 2000 *J. Catal.* **189** 129-46
[60] Lauritsen J V, Nyberg M, Vang R T, Bollinger M V, Clausen B S, Topsøe H, Jacobsen K W, Besenbacher F, Lægsgaard E, Nørskov J K and Besenbacher F 2003 *Nanotech.* **14** 385-9
[61] Lauritsen J V, Bollinger M V, Lægsgaard E, Jacobsen K W, Nørskov J K, Clausen B S, Topsøe H and Besenbacher F 2004 *J. Catal.* **221** 510-22
[62] Walton A S, Lauritsen J V, Topsøe H and Besenbacher F 2013 *J. Catal.* **308** 306-18
[63] Bollinger M V, Lauritsen J V, Jacobsen K W, Nørskov J K, Helveg S and Besenbacher F 2001 *Phys. Rev. Lett.* **87** 196803
[64] Schweiger H, Raybaud P, Kresse G and Toulhoat H 2002 *J. Catal.* **207** 76-87
[65] Bollinger M V, Jacobsen K W and Nørskov J K 2003 *Phys. Rev. B* **67** 085410
[66] Bruix A, Lauritsen J V and Hammer B 2017 *arXiv:1805.01244*

TOC graphics